Reduced-Dynamic Filtering for GNSS-Only Orbit Determination in Cislunar Space: An Experimental Assessment with LuGRE Data

Reduced-Dynamic Filtering for GNSS-Only Orbit Determination in Cislunar Space: An Experimental Assessment with LuGRE Data

Ilaria Cossu[1], Oliviero Vouch[1], Alex Minetto[1], Fabio Dovis[1], Mario Musmeci[2], Claudia Facchinetti[2]

[1]*Department of Electronics and Telecommunications (DET), Politecnico di Torino, Turin, Italy*
[2]*Agenzia Spaziale Italiana (ASI), Rome, Italy*

BIOGRAPHY

Ilaria Cossu received the M.Sc. degree (2025) in aerospace engineering from Politecnico di Torino. She is currently a researcher at the Navigation Signal Analysis and Simulation (NavSAS) group. Her research focuses on the development and application of Bayesian filtering techniques for GNSS-based orbit determination and time synchronization in cislunar space.

Oliviero Vouch received the M.Sc. degree (2020) and the Ph.D. degree (2025) in telecommunications engineering from Politecnico di Torino, Turin, Italy. He is currently a postdoctoral researcher with the Department of Electronics and Telecommunications and a member of the NavSAS research group. In 2023, he was a Visiting Doctoral Researcher at the German Aerospace Center (DLR). His research focuses on Bayesian estimation methods for multisensor integrated navigation systems based on GNSS, as well as autonomous orbit determination techniques for cislunar missions.

Alex Minetto received the M.Sc. (2015), and Ph.D. (2020) in telecommunications and electrical engineering from Politecnico di Torino, where he is now Assistant Professor in the Department of Electronics and Telecommunications and a member of the NavSAS research group. His work focuses on advanced GNSS signal analysis, receiver design, and Bayesian state estimation. He has contributed to ESA and EUSPA projects and has been involved in the Lunar GNSS Receiver Experiment (LuGRE) as a mission's Science Team member.

Fabio Dovis received the M.Sc. (1996) and Ph.D. (2000) from Politecnico di Torino, where he is now Full Professor in the Department of Electronics and Telecommunications, coordinator of the NavSAS Research Group and is Co-PI of the LuGRE project. His research focuses on GNSS receiver design, advanced signal processing for interference and multipath mitigation, and ionospheric monitoring. He has extensive experience in international projects, collaborations with industry and research institutions, and serves on the IEEE AESS Navigation Systems Panel.

Mario Musmeci received a degree in physics from the University of Rome "La Sapienza." He has worked with major Italian space companies, ESA, and the European Commission on the Galileo program, and co-founded a start-up exploiting a patent based on Galileo signals for reliable traceability of "Made in Italy" products. Since 2016, he has been with ASI's Programs Directorate, serving as technical manager for LuGRE on NASA's Firefly Blue Ghost mission, demonstrating GNSS reception on the lunar surface.

Claudia Facchinetti is a researcher and technologist at the Italian Space Agency (ASI), specializing in Earth observation and space navigation technologies. She holds a Ph.D. in Space Science and Technology and has contributed to numerous scientific projects and space missions, including studies on SAR radar and hyperspectral sensors. She is a key member of the LuGRE (Lunar GNSS Receiver Experiment) team, a joint NASA-ASI initiative that successfully demonstrated GNSS-based navigation on the Moon during the Firefly Blue Ghost Mission 1 in 2025. Additionally, she is responsible for developing Earth observation missions at ASI.

ABSTRACT

Global Navigation Satellite Systems (GNSSs) are emerging as a key enabler for autonomous Positioning, Navigation and Timing (PNT) beyond the operational limits of the Space Service Volume (SSV), supporting the increasing demand for onboard navigation in lunar exploration missions. As deep-space operations still rely heavily on ground-based tracking assets, the development of reliable onboard Orbit Determination and Time Synchronization (ODTS) becomes essential. In this context, reduced-dynamic filtering can preserve solution continuity under sparse GNSS visibility better than purely kinematic approaches, while offering robustness against dynamic mismodeling.

This work presents the first experimental assessment of GNSS-only reduced-dynamic ODTS in cislunar space using real spaceborne data from Lunar GNSS Receiver Experiment (LuGRE). Raw pseudorange and Doppler-shift data, recorded by

the GNSS payload during three representative operations along the Earth–Moon trajectory and on the lunar surface, are processed using a first-order Extended Kalman Filter (EKF) architecture. To account for the different deep-space perturbation environments across the Earth–Moon system, the ODTS filter incorporates a distance-adaptive lunar gravity model, ensuring physical consistency across Earth–Moon regimes while remaining computationally feasible for onboard use.

The results obtained across the three LuGRE operations, spanning geocentric distances from 15.03 to 51.69 Earth radii (RE) and including one surface operation, demonstrate the viability of pseudorange-based reduced-dynamic filtering for cislunar ODTS despite poor satellite geometry and depleted observability. In the most favorable near-Earth scenario, the 3D position error reaches $1.36\,\mathrm{km}$ at the 95th percentile. In the more challenging cislunar and lunar-surface cases, where only $20\,\%$ to $21\,\%$ of the operation time provides at least four tracked GNSS satellites, the orbit estimation accuracy remains within $3.91\,\mathrm{km}$ at the 95th percentile. Velocity errors remain below $1\,\mathrm{m\,s^{-1}}$ across all operations, confirming that the proposed filtering strategy can yield deep-space ODTS solutions even under degraded conditions.

I. INTRODUCTION

Recent advances in spaceborne receiver technology have significantly expanded the role of Global Navigation Satellite System (GNSS)-based Orbit Determination and Time Synchronization (ODTS) for missions beyond Earth's orbit. Outside the boundaries of the Space Service Volume (SSV), GNSS is increasingly regarded not only as a complement to traditional navigation systems, but as a key enabler of onboard autonomy for deep-space missions (Winternitz et al., 2019). In parallel, the extension of GNSS capabilities into cislunar space has emerged as a strategic frontier for satellite-based Positioning, Navigation and Timing (PNT), supporting the growing set of scientific and exploration missions envisioned in the Earth–Moon system. This perspective aligns with the Artemis Accords, which are fostering international efforts toward standardized cislunar PNT services, including the LunaNet interoperable architecture (Israel et al., 2020).

As an onboard capability, GNSS offers several transformative advantages. It reduces reliance on ground-based tracking infrastructures, which are increasingly limited by operational costs, resource availability, round-trip delays, and visibility gaps in deep-space environments. Moreover, GNSS provides precise time transfer directly from satellite clocks, eliminating the need for onboard atomic clocks and improving synchronization across Guidance, Navigation & Control (GNC) subsystems. Furthermore, GNSSs will serve as a complementary PNT backbone for prospective lunar navigation infrastructures.

Despite this promising outlook, the Earth–Moon environment, particularly at lunar altitudes, represents an extreme testbed for GNSS payloads. Only satellites on the Earth's far side are visible to a nadir-pointing antenna, with the Line-of-Sight (LoS) frequently obstructed by Earth, leading to long intervals of reduced visibility. Furthermore, severe free-space losses significantly attenuate the received signals. Although the measurement quality remains comparable to that achieved on Earth (Parker et al., 2025b), GNSS-based navigation performance is nonetheless severely degraded by the unfavorable distribution of visible satellites. The resulting geometry increases the collinearity of the LoS vectors and produces high and fluctuating Geometric Dilution Of Precision (GDOP). Under these conditions, the radial component of the ODTS solution becomes strongly coupled to the receiver clock bias, and the limited geometric diversity leads to less stable and less precise ODTS estimates compared to lower-altitude scenarios.

In this context, sequential Bayesian filters embedding an orbital propagator (i.e., orbital filters) become essential. By numerically integrating the spacecraft (S/C) equations of motion under modeled perturbations, the propagator constrains the trajectory between successive GNSS updates, maintaining physical consistency with the actual dynamics. Two features of orbital filters are particularly critical for high-altitude GNSS: (i) the ability to preserve solution continuity through GNSS outages or sparse visibility, and (ii) the reduced dependence of the ODTS estimates on instantaneous observability, which mitigates the impact of poor satellite geometry. Several model-based studies and simulation analyses with hardware-in-the-Loop (HIL) have shown that GNSS-only filtered ODTS can achieve meaningful performance across translunar trajectories and up to lunar altitudes. Early work by Capuano et al. (2016) demonstrated an Extended Kalman Filter (EKF)-based orbital filter for lunar transfer orbits, while the more recent study in Vouch et al. (2024) compared a sigma-point orbital filter with the classical EKF-based implementation for low lunar orbit navigation.

The accuracy of dynamical ODTS strongly depends on the fidelity of the force model used in the orbital propagator. Ideally, the model should characterize S/C motion with an accuracy comparable to that of GNSS measurements, a requirement that is challenging to meet in real operational scenarios. A trade-off is offered by the reduced-dynamic approach (Montenbruck, 2017), where the orbital filter is augmented with pseudo-stochastic parameters (also known as empirical accelerations) to absorb dynamic mismodeling. This strategy improves robustness and estimation accuracy while keeping the computational burden manageable. Reduced-dynamic filtering has been widely validated on real spaceborne GNSS data for near-Earth missions, and was first demonstrated in simulation for cislunar trajectories by Capuano et al. (2017). However, its actual performance in the cislunar environment has not yet been demonstrated experimentally.

This work addresses this gap by presenting the first experimental assessment of pseudorange-based reduced-dynamic ODTS

by post-processing raw GNSS observables acquired by the Lunar GNSS Receiver Experiment (LuGRE) throughout Firefly Aerospace's Blue Ghost Mission 1 (BGM1). LuGRE, a joint National Aeronautics and Space Administration (NASA)-Italian Space Agency (ASI) experiment, was conceived as the first in-flight demonstration of GNSS usage in cislunar space and on the lunar surface (Parker et al., 2025b, 2022). The payload is built around Qascom's QN400-SPACE, a high-sensitivity GPS/Galileo L1/L5 receiver specifically tailored to deep-space applications (Fantinato et al., 2022; Tedesco et al., 2023). When operated in Real-Time Processing (RTP) mode, together with the real-time navigation fixes computed from both filtered and single-point dual-constellation Position, Velocity, and Timing (PVT) estimates, the GNSS payload recorded observables from the tracked signals during in-flight and surface operations.

The analysis, which extends the core investigations baselined in the LuGRE science plan (Konitzer et al., 2024) and discussed in Parker et al. (2025b), selects three representative LuGRE mission datasets (Parker et al., 2025a):

- OP1_0, the first scientific activity during payload commissioning at an initial altitude from Earth of 15.03 Earth radii (RE);
- OP5_0, collected during the Earth-Moon transit trajectory in the first phasing orbit, where the GNSS payload was operated at an initial altitude of 51.69 RE and achieved a single-point navigation fix at $329\,982\,\mathrm{km}$;
- OP78_1, executed during surface operations just before loss of power to the lander, during which the payload computed the farthest-ever GNSS-only single-point navigation fix at approximately $398\,350\,\mathrm{km}$ (62.45 RE) from the Earth's surface.

For each dataset, measurements are filtered using a first-order EKF. The latter represents the most lightweight and well-established filter for sequential ODTS in spaceborne GNSS applications, and it has a long heritage in real-time Precise Orbit Determination (POD) of near-Earth orbiters (Montenbruck et al., 2021; Mao et al., 2021; Selvan et al., 2023). The EKF is particularly suited to the stringent onboard processing constraints imposed by the limited computational resources available in space-qualified processors. This choice therefore reflects a balance between estimation performance and computational feasibility for onboard use, compared to more demanding nonlinear filtering approaches.
It is worth remarking that the algorithm presented in this work is entirely unrelated to the POD algorithm implemented in the onboard payload. These investigations have been conducted in full independence from the payload design, architecture, and operational characteristics. No elements of the payload's proprietary processing chain, models, or implementation details have been disclosed, referenced, or derived in the development of the proposed ODTS method.

The remainder of the paper is organized as follows. Section II shortly reviews GNSS-based ODTS methods and presents the baseline formulation of S/C dynamics within the orbital propagator. Section III details the reduced-dynamic filtering strategy and its associated state space formulation, with particular emphasis on the adaptation of the force model to the lunar environment. Section IV presents the experimental results obtained from the post-processed LuGRE datasets. Eventually, Section V summarizes the main findings of this work and discusses future directions.

II. BACKGROUND

In the GNSS literature, three approaches are considered to solve the ODTS problem (Montenbruck, 2017; Capuano, 2016):

- the (purely) kinematic approach, where the S/C orbit and the receiver clock states are regressed at each epoch using only observational data, without incorporating a dynamic model (i.e., a point positioning method);
- the dynamic approach, where the S/C orbit is propagated by numerically integrating the S/C equations of motion under known perturbing forces and refined upon availability of observational data;
- the reduced-dynamic approach, which improves the former strategy via dynamic model compensation, estimating empirical accelerations to capture dynamic mismodeling.

Kinematic ODTS solutions are typically computed through single-epoch estimators (Vouch et al., 2025), whereas dynamic-model-based approaches rely on sequential Bayesian estimators, which filter measurements with the propagated dynamics to maintain physical consistency with the orbit and improve solution continuity.

1. Space Vehicle Dynamics

The dynamic evolution of the S/C orbit as modeled in the orbital propagator can be expressed with a nonlinear, first-order stochastic differential equation driven by white noise:

$$\dot{\mathbf{x}}_{\mathrm{sc}}(t) = \mathbf{f}(\mathbf{x}_{\mathrm{sc}}(t), t) + \boldsymbol{\nu}(t) \tag{1}$$

where $\mathbf{x}_{\mathrm{sc}}(t) = \left[\mathbf{r}(t)^\top \ \dot{\mathbf{r}}(t)^\top\right]^\top$ collects the kinematic states determining the instantaneous S/C orbit and the driving noise term $\boldsymbol{\nu}(t)$ captures inaccuracies in the physics-based model of orbital forces used to predict S/C inertial acceleration.

Although the orbital motion is more accurately represented in continuous-time, observations are available to the sequential estimator at discrete-time instants. Starting from an estimate of the S/C state at t_{k-1}, the initial value problem

$$\mathbf{x}_{\mathrm{sc},k} = \mathbf{x}_{\mathrm{sc},k-1} + \int_{t_{k-1}}^{t_k} \mathbf{f}(\mathbf{x}_{\mathrm{sc}}(t), \tau)\, d\tau + \boldsymbol{\nu}_k. \tag{2}$$

is solved,requiring the numerical integration of the equation (1) between measurement updates. Although a variety of methods are applicable for the solution of the equation (2), this work relies on a standard fourth-order Runge-Kutta (RK4) integrator (Montenbruck, 2017).

Following a two-body model within the Newtonian framework, the translational dynamics of the S/C in a geocentric, inertial reference can be derived from the gradient of the gravitational potential:

$$\ddot{\mathbf{r}}_{Earth} = \nabla_{\mathbf{r}} U_e = \nabla_{\mathbf{r}} \frac{\mu}{r}\,, \tag{3}$$

where $\mu = GM_E$ is the Earth's gravitational parameter and $r = \|\mathbf{r}\|_2$ is the S/C's radial distance in the Geocentric Celestial Reference System (GCRS), also known as Earth-Centered Inertial (ECI). For ease of notation, the explicit dependence on time is omitted in the following expressions. Equation (3) models the unperturbed Keplerian orbit and assumes that the Earth is gravitationally equivalent to point mass. To obtain a more realistic description of the Earth's gravitational pull, the effects of the planet's mass asymmetry must be considered. The geopotential expression can be generalized to an arbitrary distribution of mass by combining all the contributions to the potential created by individual mass elements $dm = \rho(\mathbf{s}) ds_x ds_y ds_z$ as follows:

$$U_e = G \iiint \frac{\rho(\mathbf{s}) ds_x ds_y ds_z}{\|\mathbf{r} - \mathbf{s}\|_2}\,, \tag{4}$$

where $\rho(\mathbf{s})$ is the mass density associated with an element of infinitesimal mass dm at inertial position $\mathbf{s}$, $ds_x ds_y ds_z$ is the volume of the mass element, and $\|\mathbf{r} - \mathbf{s}\|_2$ is the S/C's distance from such point.
The inverse of the distance can be expanded in a series of Legendre polynomials of degree n and order m, until obtaining

$$U_e = \frac{\mu}{R_e} \sum_{n=0}^{\infty} \sum_{m=0}^{n} \left(C_{nm} V_{nm} + S_{nm} W_{nm}\right), \tag{5}$$

where R_e is the mean Earth's equatorial radius. The geopotential coefficients C_{nm} and S_{nm}, derived from EGM-96 gravity model (Lemoine et al., 1997), describe the geopotential dependence on the Earth's mass distribution. In particular:

- for $m = 0$ the zonal coefficients C_{n0} represent the portion of the Earth's gravitational potential that is independent of longitude and for these values the general notation is $J_n = -C_{n0}$, while the corresponding S_{n0} coefficients are always zero;
- the coefficients C_{nm} and S_{nm} cannot be directly calculated because the Earth's internal mass distribution is unknown. They have instead been determined from satellite tracking observations, surface gravimetry, and altimetry data.

V_{nm} and W_{nm} satisfy the recurrence relations of the Legendre polynomials, which allows for efficient computation of the potential. The inertial acceleration contribution arising from the nonspherical harmonics of the Earth's gravitational field is expressed in the International Terrestrial Reference System (ITRS), and it must be transformed to GCRS for numerical orbit integration. For distances above $50\,000\,\mathrm{km}$, the Earth's gravitational field can be approximated as the central term plus the J_2 harmonic (Montenbruck and Gill, 2000).

In addition to the Earth's gravitational potential, other perturbative contributions must be considered in the dynamical model. Third body effects, mainly from the Moon and the Sun gravity within the Earth-Moon system, play a significant role. Assuming a generic set of n_c celestial bodies treated as point masses, this inertial acceleration is given by

$$\ddot{\mathbf{r}}_{3\mathrm{B}} = \sum_{j=1}^{n_c} \mu_j \left(\frac{\mathbf{s}_j - \mathbf{r}}{\|\mathbf{s}_j - \mathbf{r}\|_2^3} - \frac{\mathbf{s}_j}{\|\mathbf{s}_j\|_2^3} \right)\,. \tag{6}$$

The first term inside the parentheses, known as the direct effect, represents the acceleration exerted on the S/C by the gravitational potential of the j-th third body. The second term is referred to as the indirect effect and it considers the acceleration of the Earth induced by the same third body. This correction is necessary to ensure that the formulation is consistent with the GCRS. The $\mathbf{s}_j$ term denotes the position vector of the j-th third body expressed in the GCRS.
Accurate solar and lunar ephemerides are recovered from the JPL Development Ephemerides (DE) series (specifically, DE441 for this study), which provide data records of coefficients for the Chebyshev polynomial fitting of the positions and velocities of solar system bodies. In these ephemerides, the lunar coordinates are expressed with respect to the Earth's center, while the Sun's position can be derived from its barycentric vector, i.e., its position with respect to the International Celestial Reference System (ICRS). The values of the planetary mass parameters used in DE441 are provided in Park et al. (2021).

Aside from gravitational perturbations, orbital motion is also determined by surface forces, which introduce a dependence on the mass and surface structure of the orbiting vehicle. For cislunar navigation, the dominant surface force is solar radiation pressure (SRP). It results from the transfer of momentum through impact, reflection, absorption and re-emission of photons. Assuming that the direction normal to the S/C cross-sectional area A exposed to solar energy is parallel to the S/C-to-Sun LoS, the acceleration is approximated by the following cannonball model:

$$\ddot{\mathbf{r}}_{\mathrm{SRP}} = -P_{\mathrm{SRP}} \left(\frac{1\,\mathrm{AU}}{\|\mathbf{r}_s - \mathbf{r}\|_2} \right)^2 \frac{A}{m} C_R \nu_s \frac{\mathbf{r}_s - \mathbf{r}}{\|\mathbf{r}_s - \mathbf{r}\|_2} \,, \tag{7}$$

where $P_{\mathrm{SRP},\,1\mathrm{AU}} \approx 4.56 \times 10^{-6}\,\mathrm{N\,m^{-2}}$ represents the nominal solar radiation pressure at one astronomical distance from the Sun, m denotes the S/C mass, and C_R is the radiation pressure coefficient. In particular, $C_R = 1 + \varepsilon$, where ε is the fraction of the incident solar radiation reflected by the S/C's surface. The vector $\mathbf{r}_s$ corresponds to the geocentric position of the Sun, while the factor $\left(\frac{1\,\mathrm{AU}}{\|\mathbf{r}_s - \mathbf{r}\|_2} \right)^2$ accounts for the inverse-square variation of solar flux with distance. The dimensionless parameter ν_s is the shadow function, introduced to model eclipse conditions: it assumes a value of 1 when the S/C is in full sunlight, 0 during umbra (total shadow), and an intermediate value $0 < \nu_s < 1$ within the penumbra region.

In addition to the above perturbations, an orbital propagator can include the effects of atmospheric drag and thrust acceleration. Nevertheless, these effects are not considered in this model, as atmospheric drag is not relevant to the cislunar environment and LuGRE payload operations were not allocated during thrusting maneuvers of the BGM1 lander.

The total S/C inertial acceleration can thus be expressed as

$$\ddot{\mathbf{r}} = \ddot{\mathbf{r}}_{Earth} + \ddot{\mathbf{r}}_{\mathrm{3B}} + \ddot{\mathbf{r}}_{\mathrm{SRP}} \,. \tag{8}$$

These perturbative accelerations, which formalize the nonlinear transitional function in equation (1) for the second-order terms, are included in the baseline orbital propagator model used for the ODTS filter prediction step.

III. METHODOLOGY

The proposed ODTS solution is implemented through an EKF-based orbital filter formulated within a reduced-dynamic framework (Schmidt, 1967; Montenbruck et al., 2005). In this approach, the deterministic S/C dynamics are augmented with stochastic acceleration terms that compensate for force-model mismatches and unmodeled perturbations, thereby improving robustness against force model uncertainties (Bar-Shalom et al., 2001).

A key aspect of the formulation concerns the treatment of the lunar gravitational environment, which becomes a dominant perturbation for the LuGRE in-flight datasets, especially those acquired within the Moon's sphere of influence (SOI). To ensure consistency across the wide range of altitudes spanned by the mission, the lunar gravity potential is modeled through an adaptive non-spherical representation whose fidelity varies with the S/C–Moon distance. This strategy preserves high accuracy in the near-lunar region while maintaining computational efficiency in the far-field domain.

1. Reduced-Dynamic Modeling Strategy and State Space Formulation

In GNSS-based ODTS, the starting point for a dynamic formulation is the classical state vector

$$\mathbf{x}_k = \begin{bmatrix} \mathbf{x}_{\mathrm{sc},k}^\top & \mathbf{x}_{\mathrm{clk},k}^\top \end{bmatrix}^\top \in \mathbb{R}^{n \times 1}, \tag{9}$$

where $\mathbf{x}_{\mathrm{sc},k} \in \mathbb{R}^{6\times 1}$ includes the S/C position and velocity components at epoch t_k, while $\mathbf{x}_{\mathrm{clk},k}$ contains the receiver clock bias and drift parameters. In this baseline state formulation, the number of states is $n = 8$.

Although this state representation is suitable for pseudorange-based dynamic ODTS, physical force models cannot reproduce the actual S/C dynamics with accuracy comparable to that of onboard GNSS measurements. Dynamic Model Compensation (DMC) addresses this issue by introducing *pseudo-variables* that inflate the predicted covariance when force-model uncertainty is high, thereby compensating for unmodeled perturbations and model imperfections (Schmidt, 1967).

In the reduced-dynamic approach, these pseudo-variables take the form of empirical (also known as stochastic) accelerations. Following Bar-Shalom et al. (2001) and Capuano et al. (2017), their temporal evolution is not modeled as white noise but as a first-order Gauss–Markov (Ornstein–Uhlenbeck) process with exponential autocorrelation

$$R(\tau) = E[\mathrm{a}_{emp}(t)\mathrm{a}_{emp}(t+\tau)] = \sigma_a^2 e^{-\alpha\tau}, \quad \alpha > 0\,, \tag{10}$$

where σ_a^2 is the steady-state variance of the process, and α^{-1} represents its correlation time. This process can be generated by a first-order dynamic system that acts as a prewhitening filter for the acceleration noise. In this representation, the process evolves according to the differential equation

$$\dot{\mathrm{a}}_{emp}(t) = -\alpha\,\mathrm{a}_{emp}(t) + w(t)\,, \tag{11}$$

where $w(t)$ denotes a zero-mean driving white noise with spectral density

$$E[w(t)w(\tau)] = 2\alpha\,\sigma_a^2\,\delta(t-\tau)\,, \tag{12}$$

which ensures the autocorrelation in equation (10). A key implication of adopting an exponentially correlated process noise is the Markov property of the state is violated. To retain compatibility with standard filtering formulations within the Bayesian framework, empirical accelerations must be included explicitly in the state vector.

This leads to the augmented state

$$\mathbf{x}_k = \begin{bmatrix}\mathbf{x}_{\mathrm{sc},k}^\top & \mathbf{x}_{\mathrm{clk},k}^\top & \mathbf{a}_{\mathrm{emp},k}^\top\end{bmatrix}^\top \in \mathbb{R}^{n\times 1}, \tag{13}$$

where $\mathbf{a}_{\mathrm{emp},k}$ collects the stochastic acceleration components for each spatial dimension. This augmented formulation yields $n = 11$ states to be estimated.

This augmentation restores the Markovian representation of the hidden process, enabling the EKF to properly propagate uncertainty while maintaining a force model of moderate complexity, the latter being an essential requirement for onboard space-qualified processors with limited computational resources.

a) Measurement Model

The reduced-dynamic ODTS filter processes code-based pseudorange and Doppler-shift observations recorded by the LuGRE payload in RTP mode during the in-flight and surface operations. Before being assimilated by the EKF, the raw measurements are corrected for modeled systematic biases.

For range measurements, a dominant error contribution is the ionospheric refractive delay, particularly for satellites whose trajectories graze the Earth's limbs with ray paths that accumulate large slant delays. In the developed ODTS filter, first-order ionospheric biases are corrected as follows. When dual-frequency observables are available, the standard iono-free linear combination is applied, at the cost of increased measurement noise due to noise amplification. Otherwise, a single-frequency ionospheric correction, adapted from the formulation in (Long, 2024), is applied using the Klobuchar broadcast model, with coefficients extracted from the daily CDDIS navigation files.
Inter-system timing biases are also corrected a priori. In particular, the GPS to Galileo Time Offset (GGTO) is removed following the polynomial model from the same daily ephemeris files.

Upon compensation of modeled biases, residual measurement errors are treated as additive, zero-mean white noise with non-stationary covariance $\boldsymbol{R}_k$.
For the stochastic disturbance affecting pseudorange observations, the largest contribution to the User Equivalent Range Error (UERE) budget is receiver noise. The latter is dominated by the delay-Lock Loop (DLL) tracking jitter, whose Root-Sum-Squared (RSS) value for BPSK-modulated signals processed in a non-coherent E-L discriminator is given by (Betz and Kolodziejski, 2000):

$$\sigma_{DLL} \approx \sigma_{t,DLL} = \begin{cases} \sqrt{\frac{B_n}{2\,C/N_0}\,D\Big(1+\frac{2}{T\,C/N_0\,(2-D)}\Big)}, & D \geq \frac{\pi R_c}{B_{\mathrm{FEA}}} \\ \sqrt{\frac{B_n}{2\,C/N_0}\Big(\frac{1}{B_{\mathrm{FEA}}T_c}+\frac{B_{\mathrm{FEA}}T_c}{\pi-1}\Big(D-\frac{1}{B_{\mathrm{FEA}}T_c}\Big)^2\Big)\Big(1+\frac{2}{T\,C/N_0\,(2-D)}\Big)}, & \frac{R_c}{B_{\mathrm{FEA}}} < D < \frac{\pi R_c}{B_{\mathrm{FEA}}} \\ \sqrt{\frac{B_n}{2\,C/N_0}\,\frac{1}{B_{\mathrm{FEA}}T_c}\Big(1+\frac{1}{T\,C/N_0}\Big)}, & D < \frac{R_c}{B_{\mathrm{FEA}}} \end{cases} \tag{14}$$

where D is the correlators' spacing, B_n the code loop noise bandwidth, $T_c = 1/R_c$ is the chip time, B_{FEA} the front end filter bandwidth, and T the predetection integration time. Receiver-dependent parameters are set according to the LuGRE payload specifications (Parker et al., 2025b). For BOC-modulated signals, equation (14) is adapted following (Betz, 2000).

Doppler-shift observations are primarily affected by carrier-phase tracking errors and frequency estimation noise. For signals tracked using a third-order phase-lock loop (PLL), the RSS phase error is modeled as

$$\sigma_{PLL} = \sqrt{\sigma^2_{t,PLL} + \theta^2_{A3}}\,, \tag{15}$$

where $\sigma_{t,PLL}$ is the thermal-noise-induced jitter and θ_{A3} accounts for oscillator instability via the Allan deviation.
For frequency tracking within an frequency-lock loop (FLL), the corresponding thermal-noise contribution is instead

$$\sigma_{FLL} = \frac{\lambda_L}{2\pi T}\sqrt{\frac{4FB_n}{C/N_0}\left(1 + \frac{1}{TC/N_0}\right)}\,. \tag{16}$$

2. State Transition Matrix and Variational Equation

In the discrete-time EKF formulation, the matrix $\hat{\Phi}_{k-1}$ used in the prediction step represents a first-order approximation of the continuous-time state transition matrix over the sampling interval $\Delta t = t_k - t_{k-1}$. In the continuous domain, the state transition matrix $\mathbf{\Phi}(t, t_0)$ is defined as

$$\mathbf{\Phi}(t, t_0) = \frac{\partial \mathbf{x}(t)}{\partial \mathbf{x}(t_0)}, \tag{17}$$

where $\mathbf{x}(t_0)$ is the initial state. Equation (17) captures the effect of small variations in the initial conditions on the S/C trajectory. Differentiating the formulation (1) with respect to the initial state, it is possible to obtain the equation that describes the time evolution of equation (17)

$$\frac{\partial}{\partial \mathbf{x}(t_0)}\frac{d}{dt}x(t) = \underbrace{\frac{d}{dt}\frac{\partial x(t)}{\partial \mathbf{x}(t_0)}}_{\dot{\mathbf{\Phi}}(t,t_0)} = \underbrace{\frac{\partial \mathbf{f}(\mathbf{x}(t), t)}{\partial \mathbf{x}(t)}}_{\mathbf{F}(t)}\frac{\partial \mathbf{x}(t)}{\partial \mathbf{x}(t_0)} \tag{18}$$

where $\mathbf{F}(t)$ is the Jacobian matrix of the nonlinear dynamics.

The previous expression can be written compactly as

$$\dot{\mathbf{\Phi}}(t, t_0) = \mathbf{F}(t)\,\mathbf{\Phi}(t, t_0). \tag{19}$$

According with the state vector (13) and the empirical acceleration definition (11), the Jacobian $\mathbf{F}(t)$ takes the block form

$$\mathbf{F}(t) = \begin{bmatrix} \mathbf{0}_{3\times3} & \mathbf{I}_{3\times3} & \mathbf{0}_{3\times1} & \mathbf{0}_{3\times1} & \mathbf{0}_{3\times3} \\ \frac{\partial \mathbf{f}(\mathbf{x}_{\rm sc}(t),t)}{\partial \mathbf{r}} & \frac{\partial \mathbf{f}(\mathbf{x}_{\rm sc}(t),t)}{\partial \dot{\mathbf{r}}} & \mathbf{0}_{3\times1} & \mathbf{0}_{3\times1} & \mathbf{I}_{3\times3} \\ \mathbf{0}_{1\times3} & \mathbf{0}_{1\times3} & 0 & 1 & \mathbf{0}_{1\times3} \\ \mathbf{0}_{1\times3} & \mathbf{0}_{1\times3} & 0 & 0 & \mathbf{0}_{1\times3} \\ \mathbf{0}_{3\times3} & \mathbf{0}_{3\times3} & \mathbf{0}_{3\times1} & \mathbf{0}_{3\times1} & -\alpha\,\mathbf{I}_{3\times3} \end{bmatrix}. \tag{20}$$

Here, the block $\dfrac{\partial \mathbf{f}(\mathbf{x}_{\rm sc}(t), t)}{\partial \dot{\mathbf{r}}}$ has been set to $\mathbf{0}_{3\times3}$ since the deterministic acceleration model adopted in this work does not depend on velocity, while $\dfrac{\partial \mathbf{f}(\mathbf{x}_{\rm sc}(t), t)}{\partial \mathbf{r}}$ represents the partial derivatives of the acceleration with respect to the position. The explicit expressions of these derivatives depend on the adopted force models, and their implementation follows the formulation discussed in detail in Montenbruck and Gill (2000).

The discrete-time transition matrix used in the EKF is then obtained by integrating the equation (19) over the time interval Δt.

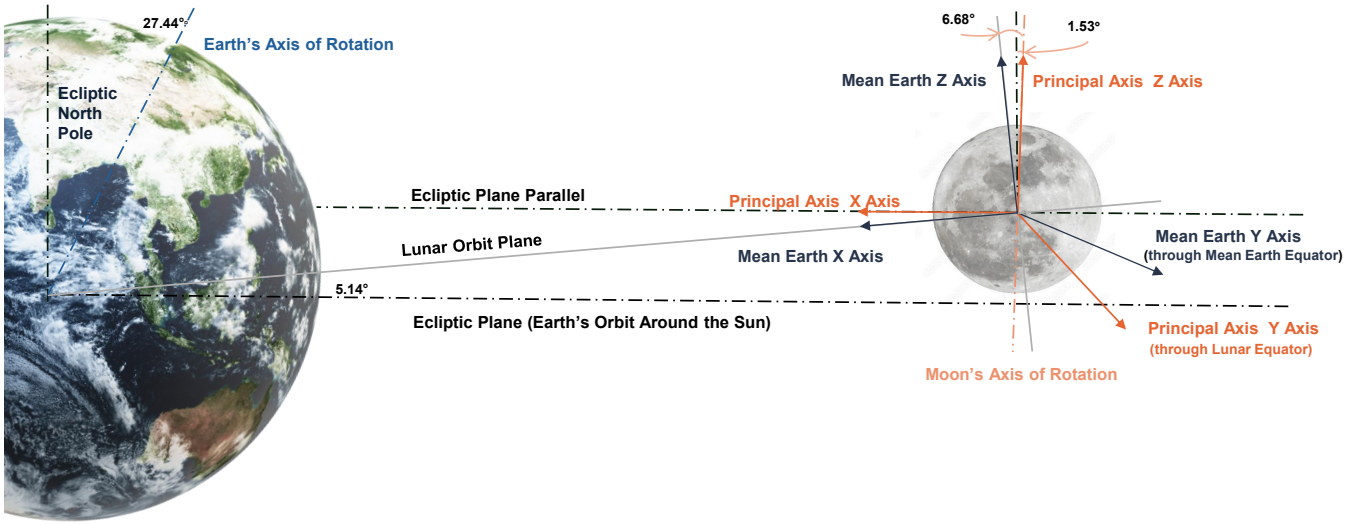

Figure 1: Simplified diagram highlighting differences between lunar reference frames. Reproduced from NASA (2024).

3. Orbital Dynamics Modelling in the Lunar Vicinity

The in-flight datasets processed in this study span two distinct dynamical regimes within the Earth–Moon system. The commissioning operation OP1_0 during the first Earth-Moon phasing loop was executed in a region well inside the Earth's SOI, where the Moon acts primarily as a third-body perturbation. In such scenario, the geocentric inertial dynamical model described in Section II.1 remains suitable in the orbital propagator. Transit operation OP5_0, instead, was acquired at an initial geocentric distance of 51.69 RE prior to apogee maneuver, placing the S/C near the outer boundary of the Moon's SOI (i.e., a radius of approximately $66\,000\,\mathrm{km}$ from the Moon's center). In this transition region, while a geocentric dynamical formulation remains appropriate, lunar gravity becomes comparable to the terrestrial perturbation on the orbiting S/C and cannot be represented as a point-mass term alone.

To ensure an accurate and dynamically consistent treatment across both regimes, the geocentric inertial model in the orbital propagator is extended by incorporating a non-spherical representation of the lunar gravitational potential. The lunar gravity field is modeled through a spherical harmonic expansion whose degree and order vary with the S/C–Moon distance. By default, a 20×20 model is employed, where harmonics coefficients are extracted from AIUB-GRL350A gravity (Bertone et al., 2021). For distances greater than $50\,000\,\mathrm{km}$, the expansion is truncated at the fourth zonal coefficient (i.e., J_4), and beyond the SOI's outer boundary only the J_2 term is retained.

All non-spherical gravity computations are performed in the lunar body-fixed Principal Axis (PA) reference system, whose axes align with the principal moments of inertia. Although the older mean Earth (ME)/polar axis reference system is widely adopted for cartographic distribution and surface-related products, the PA system is generally preferred for orbital dynamics because it diagonalizes the inertia tensor and simplifies the gravity-field formulation (NASA, 2024). The choice of the PA system is also aligned with ongoing developments within ESA's Moonlight programme and the broader Lunar Communications and Navigation Services (LCNS) framework, which propose the establishment of a kinematically non-rotating lunar inertial frame together with a consistent Moon-fixed frame for future navigation and timing services (Iess et al., 2025). Eventually, the transformation between PA coordinates and the ICRS is performed using a triplet of Euler angles, ϕ, θ and ψ, obtained from JPL DE441 series, which describe the Moon's physical libration.

a) Dynamical Model Adaptation for Surface Positioning

For the post-processing of OP78_1 dataset, acquired while the BGM1 lander was stationary on the lunar surface, the dynamical model must be adapted to reflect the fundamentally different motion regime compared to in-flight operations.
Although the state vector formulation (13) for reduced-dynamic filtering is kept unchanged, the physical interpretation of the dynamic model and of the empirical accelerations differs significantly.

Since the lander is static with respect to the Moon, the perturbation-driven orbital propagator used for in-flight ODTS is not applicable. Instead, the state propagation adopts a simplified coordinate-uncoupled stochastic model tailored to static positioning. S/C kinematics in the PA frame are represented as a nearly constant-acceleration model driven by a small white-jerk process

noise (Bar-Shalom et al., 2001). In the discrete-time state space formulation, this corresponds to a second-order polynomial model with independent increments, in which the empirical acceleration states act as random-walk terms rather than first-order Gauss–Markov processes.

In this context, the empirical acceleration terms no longer compensate for unmodelled or mismodelled orbital forces, as they do in the in-flight reduced-dynamic model. Instead, the absorb residual errors arising from (i) model inaccuracies in the JPL DE series used to extract the Moon's physical libration angles and their rates, (ii) numerical errors in the ICRS-PA transformation, and (iii) deviations between the true lunar rotational dynamics and their analytical representation.
This adaptation enables the prediction model to remain consistent with the stationary nature of the surface scenario while preserving a unified state formulation across all experimental datasets.

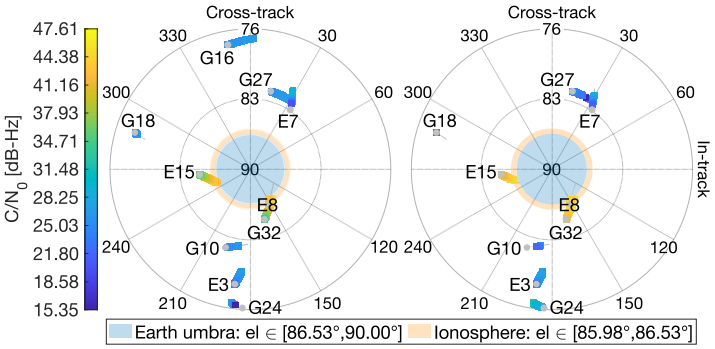

(a) OP1_0: space skyplot. L1 C/A/E1C (left) and L5/E5a-Q (right).

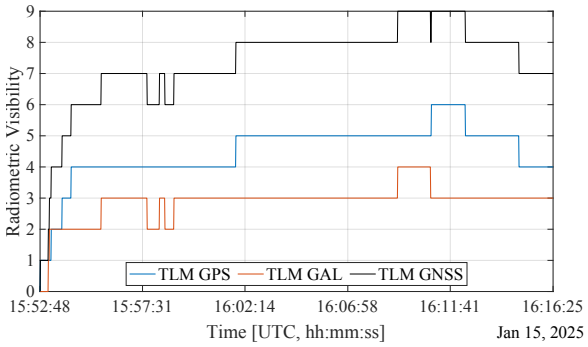

(b) OP1_0: single-/multi-constellation visibility (unique SVs).

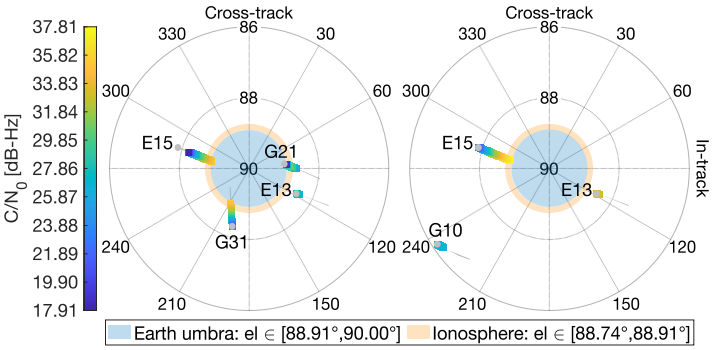

(c) OP5_0: space skyplot. L1 C/A/E1C (left) and L5/E5a-Q (right).

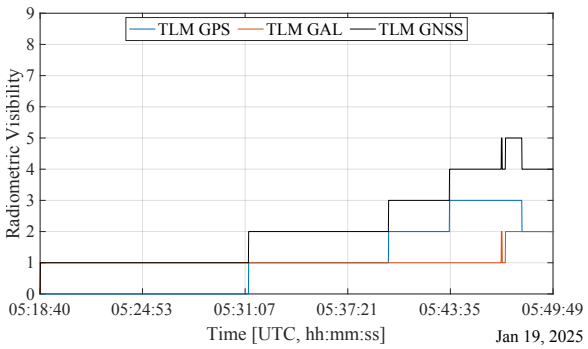

(d) OP5_0: single-/multi-constellation visibility (unique SVs).

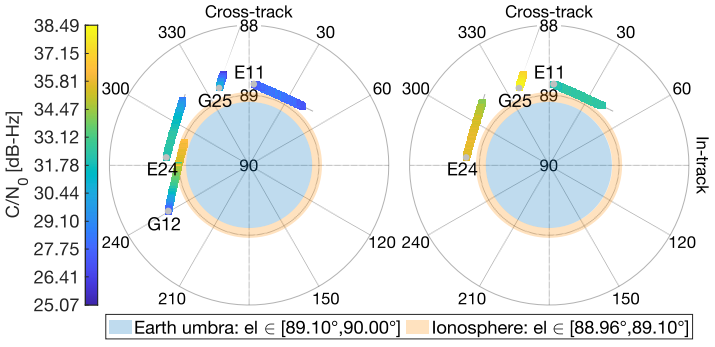

(e) OP78_1: space skyplot. L1 C/A/E1C (left) and L5/E5a-Q (right).

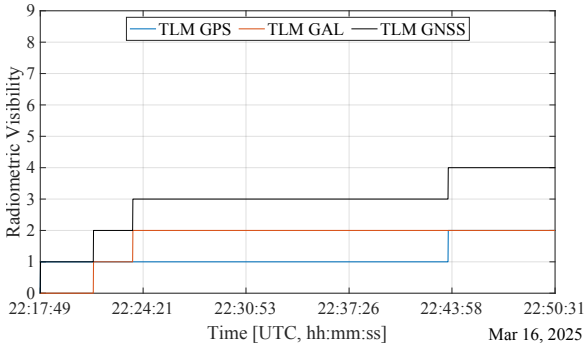

(f) OP78_1: single-/multi-constellation visibility (unique SVs).

Figure 2: Space skyplots (left column) and corresponding radiometric visibility timeseries (right column) for the three analyzed LuGRE operations. C/N_0 levels of tracked satellites are extracted from onboard signal strength measurements by the LuGRE payload.

IV. RESULTS

This section presents the results obtained by applying the reduced-dynamic filtering strategy described in Section III to the three selected LuGRE operations. In all cases, the reduced-dynamic dynamical model is implemented through a first-order EKF, which is used here as a representative and computationally lightweight realization of the proposed framework for sequential GNSS-only ODTS.

1. Navigation Analysis

Figure 2 summarizes the radiometric observation conditions characterizing the analyzed LuGRE mission datasets. For each operation, the left panel shows a *space skyplot*, while the right panel reports the radiometric visibility timeseries (GPS-only, Galileo-only, and combined) counted on unique satellite vehicles. In line with the onboard processing capabilities of the LuGRE payload (Tedesco et al., 2023), the post-processing algorithm is configured in dual-constellation, dual-frequency mode, exploiting GPS and Galileo observations on both L1/E1 and L5/E5a bands.

The space skyplots characterize the relative geometry between the S/C and the tracked GNSS satellites under the assumption of a nadir-pointing attitude, i.e., the LuGRE high-gain antenna (HGA) is considered to be continuously aligned with the Earth's center. Satellite orbits, retrieved in constellation-specific Earth-fixed rotating frames from broadcast ephemerides (CDDIS daily files), are transformed into the S/C local frame for the time period spanning each LuGRE operation. In this rotating orbital frame, the polar diagram represents the apparent motion of the tracked GNSS satellites as seen from the payload antenna. Each satellite trajectory is plotted as a gray line and overlaid with a C/N_0 heatmap for each tracked signal component: the left skyplot in each row corresponds to L1 C/A and E1C, while the right skyplot corresponds to L5Q and E5a-Q. C/N_0 estimates are computed by the receiver on pilot components where available, thus directly reflecting the sensitivity tracking capabilities of the LuGRE payload.
The Earth's disk and a surrounding ionospheric shell are superimposed as shaded regions, enabling a qualitative discrimination between main-lobe and side-lobe reception: stronger signals tend to cluster near the Earth's limb, whereas weaker C/N_0 values at lower apparent elevations are typically associated with side-lobe tracking. For example, Figure 2a for the low-altitude OP1_0 highlights a substantial portion of side-lobe receptions occurring above the receiver's sensitivity threshold. On the contrary, Figure 2c, for the farther transit operation OP5_0, is dominated by main-lobe tracking, with satellite trajectories intersecting the ionospheric layer while rising into radiometric view or setting behind the Earth.

The visibility timeseries on the right-hand side of Figure 2, extracted and adapted from the LuGRE quick navigation analysis and reporting tool (LuNART-q) [1] (Minetto et al., 2025), emphasize the intermittent and constellation-dependent nature of GNSS coverage during the Earth-Moon transit and on the Moon's surface, which is also highly subject to the specific time frame at which the operation took place. These trends are consistent with what is observed in the corresponding skyplots. In OP1_0 (Figure 2b), the combined presence of main-lobe and side-lobe receptions results in the availability of at least four GNSS satellites for a well-defined multilateration problem for $97.81\,\%$ of the operation duration. On the other hand, OP5_0 (Figure 2d) and OP78_ (Figure 2f) exhibit markedly reduced radiometric visibility, with at least four tracked satellites maintained for only $20.21\,\%$ and $20.78\,\%$ of the respective time spans. These results highlight how the loss of side-lobe contributions at lunar distances directly translates into sparse visibility, and ultimately into depleted observability for GNSS-based ODTS.

2. ODTS Performance and Error Statistics

For each operation, the filter is warm-started by exploiting a set of a-priori information available from the mission products and ancillary data. In particular, the initial orbit state used to initialize the EKF is extracted in post-processing from a lander trajectory delivered by the Firefly Mission Control Center within few hours after the end of each payload operation. This operational product is employed in post-processing to provide a realistic initial condition and covariance to the filter. Additional aiding information includes Earth orientation parameters (EOPs) for frame transformations and the lander physical parameters required by the force model in the orbital propagator.

Figures 3, 4, and 5 present the timeseries of the S/C's position and velocity errors expressed in the radial, in-track, cross-track (RIC) frame for the three analyzed operational scenarios. Two components are considered: the radial and the normal (lateral) directions. In each error plot, the solid lines indicate the difference between the estimated value and the true lander orbit at each sampling instant. Moreover, the shaded bands in the background represent the corresponding filter uncertainty envelopes at 3-σ, derived from the estimated posterior covariance. For the normal (lateral) component, these values are computed as the RSS of the relevant covariance terms, while for the radial component they correspond to three times the standard deviation in that direction. Each plot is combined with the corresponding GDOP values over the same time window, providing an indication of the measurement geometry that affects the estimation performance. They have been extracted from the single-epoch PVT navigation solutions of the onboard GNSS payload, and are thus available only when a minimum of four satellites are tracked.

[1] The open-source tool is publicly available at https://github.com/NavsasPolito/LuNART.

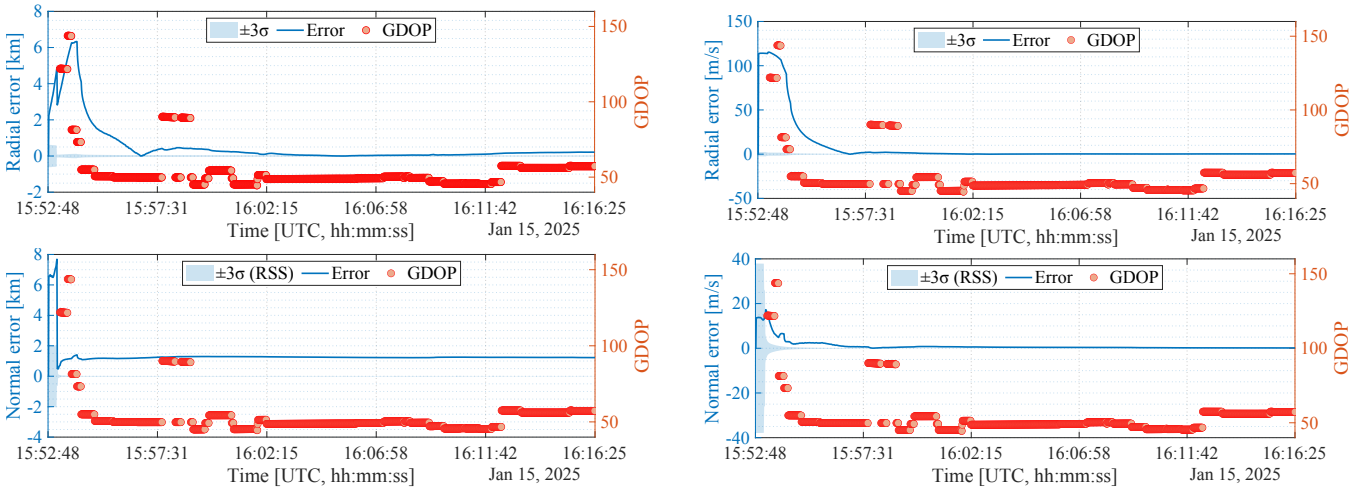

(a) Radial and lateral position error timeseries.

(b) Radial and lateral velocity error timeseries.

Figure 3: RIC-frame error decomposition for LuGRE operation OP1_0: (a) position error components; (b) velocity error components.

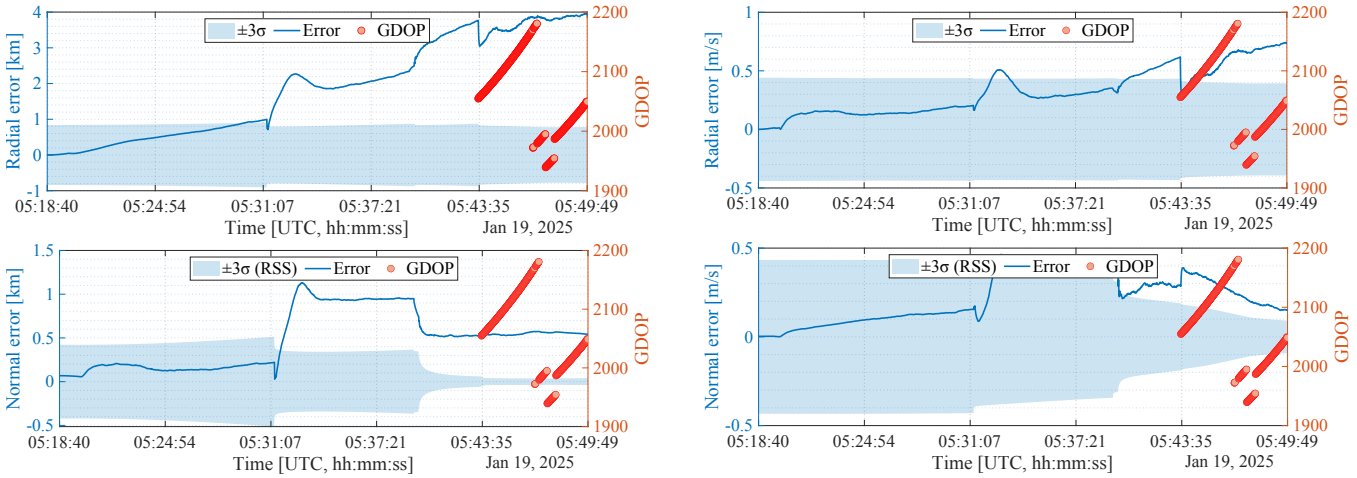

(a) Radial and lateral position error timeseries.

(b) Radial and lateral velocity error timeseries.

Figure 4: RIC-frame error decomposition for LuGRE operation OP5_0: (a) position error components; (b) velocity error components.

Starting from scenario OP1_0 in Figure 3a, both the radial and the normal position estimation errors are subject to an initial transient during the first minutes of the operation.The effect is more emphasized in the radial component, whose estimator exhibits a slower convergence than the normal one. This can be explained by the GDOP trend, which reveals a strong radial alignment of the tracked satellites, resulting in limited observability of the radial and clock states as independent components. As a consequence, their decoupling is delayed, and the radial estimate converges only once the measurement geometry improves. Once convergence is achieved, the radial error remains close to zero, with an accuracy corresponding to an Root-Mean-Square Error (RMSE) of $166\,\mathrm{m}$ and a precision of $1.5\,\mathrm{m}$. In contrast, the normal component stabilizes with an accuracy of $1.23\,\mathrm{km}$ and a precision, evaluated as an RSS, of $3.4\,\mathrm{m}$. From the previous results, it can be inferred that the estimation error lies outside the 3σ limits, indicating that the estimator is not consistent, i.e., the estimate does not converge to the true state (Bar-Shalom et al., 2001). This behavior is likely attributable to the presence of unmodeled, and therefore uncorrected, systematic errors in the measurements. A similar trend can be observed in Figure 3b, which shows the time series of the velocity error. In this case, once convergence is achieved, the filter achieves centimeter-per-second–level precision and decimeter-per-second–level accuracy in both the radial and normal directions. In particular, the radial RMSE is $0.272\,\mathrm{m\,s^{-1}}$, while the corresponding value for the normal direction is approximately $0.196\,\mathrm{m\,s^{-1}}$.

Moving to scenario OP5_0, this operation is characterized by a reduced number of tracked satellites with respect to the previous one, with an average combined GPS/Galileo visibility of 2.15 satellites over the entire operation, compared to 7.36 satellites

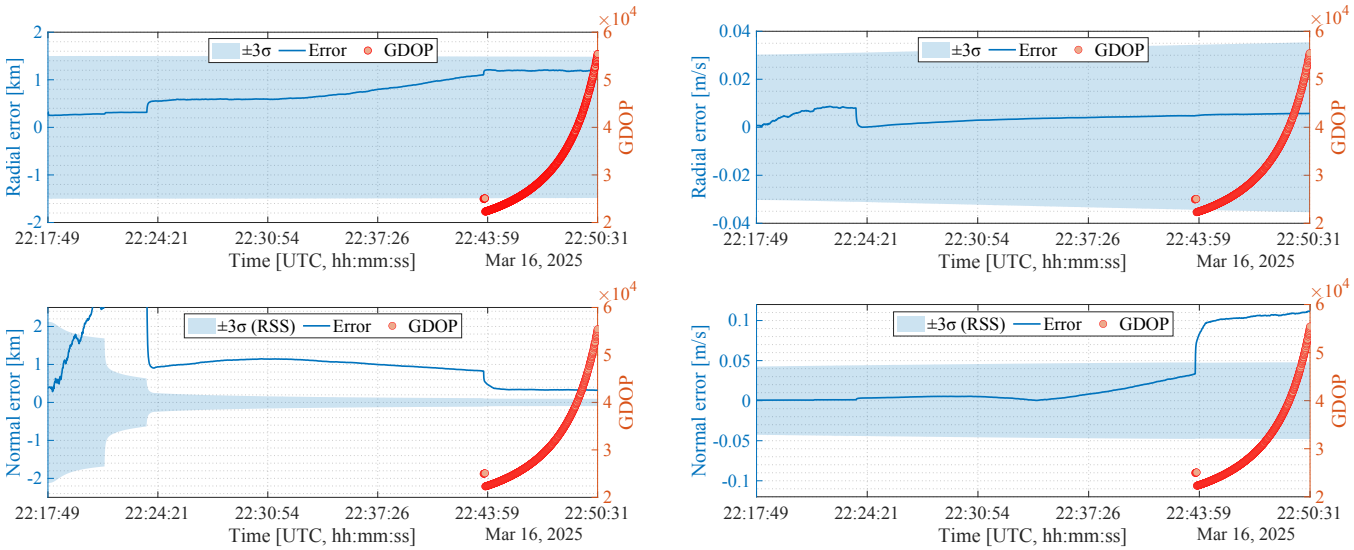

(a) Radial and lateral position error timeseries.

(b) Radial and lateral velocity error timeseries.

Figure 5: RIC-frame error decomposition for LuGRE operation OP78_1: (a) position error components; (b) velocity error components.

for the previous scenario. This reduction is reflected in the poorer precision of the estimates, as evaluated through the posterior covariance at the 3σ level When the number of tracked satellites increases to four at 05:43:35, a slight reduction in the radial error is observed, indicating a partial improvement in the radial–clock decoupling, particularly evident in the velocity estimate. Nevertheless, this enhancement in measurement availability does not lead to full radial convergence. This is due to the strong geometric collinearity among the tracked satellites at that time, as highlighted by the GDOP ramp, which limits the effective gain in observability provided by the additional measurement. As a result, the radial component is adversely affected in both position and velocity estimates, leading to a divergence of the estimator along the radial direction. In contrast, the normal position component exhibits convergence toward a biased solution, with an RMSE of $543\,\mathrm{m}$ and a precision of $19\,\mathrm{m}$. Regarding the normal velocity component, the filter appears to move toward convergence after the inclusion of the fourth satellite; however, the limited duration of the operational window does not allow the attainment of a clear steady-state condition.

Focusing on the post-landing surface scenario OP78_1, and in line with the high-altitude transit operation OP5_0, the combined average GPS/Galileo visibility is 2.92 satellites. The radial position error in Figure 5a (top) exhibits a slow and steady growth over the entire observation interval. This behavior is consistent with the absence of strong dynamical constraints in the transitional model used for surface positioning (see Section III.3 a), combined with the scarcity of navigation observables throughout the operation. Over the same time window, the posterior covariance associated with the radial component remains nearly constant, corresponding to an estimated precision of approximately $1.49\,\mathrm{km}$ (3σ). In terms of accuracy, the radial error reaching values of about $1.19\,\mathrm{km}$ in the final portion of the operation, after approximately 22:43:59.

Compared to the radial component, the normal error in Figure 5a (bottom) exhibits a higher sensitivity to variations in observability, where changes in the number of tracked satellites directly affect the amount of information available to the filter. As the operation progresses, the uncertainty estimated from the posterior covariance progressively reduces, indicating that the filter increasingly relies on the assumed motion model, characterized by a low white-noise jerk process, rather than on measurement updates. This behavior may also explain the limited sensitivity of the position estimates to the GDOP cusp observed toward the end of the operation. In correspondence with the introduction of new measurements, happening before 22:24:21 and around 22:43:59 according to Figure 2f, the normal position error reduces. This behavior suggests that the filter is effectively separating the radial and clock components, thereby enabling a convergence of the normal position estimate when additional information becomes available. Nevertheless, the estimator remains biased over the observed time window, with the true error exceeding the corresponding posterior uncertainty, indicating a loss of consistency.

Concerning velocity statistics, the lander is stationary in the PA frame during OP78_1, allowing for a tighter initialization of the covariance associated with the velocity components compared to previous operations. The radial velocity error in Figure 5b (top) exhibits a trend that is qualitatively similar to that observed for the radial position component, although its response to the introduction of new measurements is opposite. In particular, a clear reduction of the radial velocity error is observed before 22:24:21, corresponding to the start of dual-frequency tracking of Galileo PRN 11 (see Figure 2e). This indicates an immediate benefit from the increased measurement information content, which allows the filter to better decouple the radial estimate from the clock drift. The posterior covariance associated with the radial velocity component shows a slight but progressive increase, with an average precision of approximately $3.32\,\mathrm{cm\,s^{-1}}$ at the 3σ level. Despite this gradual growth in uncertainty, which is

only weakly correlated with GDOP variations, the radial velocity estimate remains consistent throughout the operation. In terms of accuracy, the radial velocity RMSE amounts to $0.42\,\mathrm{cm\,s^{-1}}$, assessing the good quality of velocity estimation even under highly-reduced observability conditions. The radial velocity error remains close to zero but shows a slight deviation during the operation.

As noted earlier, the progressive radial alignment of the tracked satellites leads to increasingly unfavorable geometric conditions in the final part of the observation window. In particular, the start of dual-frequency tracking of GPS PRN 25 (see Figure 2e) increases to four the number of available satellite for the first time during the operation, but also causes a markedly ill-conditioned measurement geometry. Therefore, the normal velocity estimate, which had remained consistent despite a gradually increasing error trend, starts to diverge. This indicates that the GDOP cusp at the end of the operation primarily affects the normal component, while the radial estimate remains comparatively robust. A plausible explanation is that the filter has already achieved an effective radial–clock decoupling, resulting in a tighter radial covariance and thus a reduced sensitivity to the information carried by the newly tracked satellite. Conversely, once the clock drift estimate has largely converged to the true value, the geometric distribution of the satellites predominantly impacts the normal direction, thereby explaining the loss of consistency in the normal velocity estimation with the associated divergence.

Table 1: Percentiles (25th, 50th, 75th, 95th) of position and velocity estimation error distributions for the analyzed LuGRE mission datasets.

	Position error [km]				Velocity error [m/s]			
LuGRE operation	P25	P50	P75	P95	P25	P50	P75	P95
OP1_0	1.25	1.26	1.29	1.36	0.27	0.42	0.76	1.97
OP5_0	0.63	2.18	3.40	3.91	0.21	0.57	0.64	0.76
OP78_1	1.23	1.33	1.36	3.36	0.058	0.085	0.17	0.19

Cumulative error statistics of the three operations are summarized in Table 1. The results highlight performance differences among the datasets. OP1_0 exhibits generally lower position errors (reaching 1.36 km at the 95th percentile), while OP5_0 and OP78_1 show significantly larger errors at the upper percentiles, indicating a strong sensitivity to the limited satellite availability and to the poor geometric distribution of the measurements, as also reflected by the GDOP trend. For the velocity estimates, OP78_1 provides the lowest errors across all percentiles. This behavior can be attributed to the different dynamic conditions characterizing this operation, since it is no longer a flight phase and the lander remains stationary with respect to the PA frame. OP1_0 instead displays noticeably higher errors at the 95th percentile, mainly due to the presence of initial outliers affecting the filter convergence. These statistics are also influenced by the specific algorithm tuning, particularly the choice of the initial covariance and the parameters used to define the process noise, which further contribute to the observed differences in the final solution accuracy among the processed datasets. These results demonstrate that, when applying the reduced-dynamic EKF across the different LuGRE operations, the number of available satellites, the poor geometry, and the degraded measurement quality significantly affect the posterior ODTS accuracy.

V. CONCLUSION

Overall, this work provides the first assessment of GNSS-only ODTS in the cislunar regime using real in-flight observables from the LuGRE payload, moving beyond the simulation-based studies reported so far. In particular, it shows that reduced-dynamic filtering with an EKF, well-established for orbital navigation in near-Earth applications, can be successfully adapted to real GNSS data for navigation in deep-space. The key findings from the experimental results can be summarized as follows:

- The three operations exhibit different radiometric conditions; compared with OP1_0, both OP5_0 and OP78_1 are affected primarily by degraded measurement geometry, driven by partial radial alignment of the tracked S/C. This unfavorable configuration reduces the effectiveness of the corrections and ultimately limits the achievable estimation accuracy.
- In OP5_0 and OP78_1, where combined GPS and Galileo visibility doesn't exceed five satellites, the EKF maintains wider covariance bounds and lower confidence in its estimates, which is consistent with the reduced measurement information available in cislunar configurations.
- Weak C/N_0 conditions and side-lobe receptions broaden the error distribution. These effects become more pronounced at lunar distances, where signal strength and geometry are jointly degraded.

Additionally, part of the observed variability can be attributed to the tuning of the reduced-dynamics filter itself, especially the choice of initial covariance and the process-noise parameterization, which becomes critical if the filter is intended for near–real-time operation. This highlights the need to further explore auto-tuning methodologies to support fully adaptive process and noise models in future developments. Results highlight both the potential and the limitations of GNSS-only solutions for orbital navigation in these challenging regimes. On the one hand, the orbital filter can provide continuous ODTS estimates

with meaningful accuracy under conditions of sparse visibility and degraded satellite geometry, offering a degree of navigation autonomy not achievable with ground-based tracking alone. On the other hand, the analysis reveals a stronger sensitivity to signal availability and occasional filter divergence, with performance levels that are less favorable than expected from previous simulation-based studies, especially at lunar altitudes. This discrepancy emphasizes the importance of experimental validation: while filtered ODTS remains promising, real data highlight challenges that were not fully captured in simulations, calling for further refinement of filter design and measurement processing. Further investigation is required to better characterize possible signal bending and atmospheric effects that may introduce unmodeled biases in the GNSS observables.

ACKNOWLEDGEMENTS

This material is based upon work funded by the contract n. 2021-26-HH.0 ASI/Politecnico di Torino "Attivita di R&S inerente alla Navigazione GNSS nello Space volume Terra/Luna nell'ambito del Lunar GNSS Receiver Experiment".

REFERENCES

Bar-Shalom, Y., Li, X. R., and Kirubarajan, T. (2001). *Estimation with Applications to Tracking and Navigation: Theory, Algorithms, and Software*, pages 319–338. John Wiley & Sons, Inc., New York.

Bertone, S., Arnold, D., Girardin, V., Lasser, M., Meyer, U., and Jäggi, A. (2021). Assessing Reduced-Dynamic Parametrizations for GRAIL Orbit Determination and the Recovery of Independent Lunar Gravity Field Solutions. *Earth and Space Science*, 8(6):e2020EA001454. e2020EA001454 2020EA001454.

Betz, J. W. (2000). Design and performance of code tracking for the GPS M code signal. In *Proceedings of the 13th International Technical Meeting of the Satellite Division of The Institute of Navigation (ION GPS 2000)*, pages 2140–2150.

Betz, J. W. and Kolodziejski, K. R. (2000). Extended theory of early-late code tracking for a bandlimited GPS receiver. *Navigation*, 47(3):211–226.

Capuano, V. (2016). *GNSS-Based Navigation for Lunar Missions*. Ph.d. thesis, École Polytechnique Fédérale de Lausanne, Lausanne, Switzerland. Thèse No. 7130, Faculty of Engineering Science and Technology, Laboratory of Electronics and Signal Processing, Doctoral Program in Microsystems and Microelectronics.

Capuano, V., Basile, F., Botteron, C., and Farine, P.-A. (2016). GNSS-based Orbital Filter for Earth Moon Transfer Orbits. *The Journal of Navigation*, 69(4):745–764.

Capuano, V., Shehaj, E., Botteron, C., Blunt, P., and Farine, P.-A. (2017). An adaptive gnss-based reduced dynamic approach for real time autonomous navigation from the earth to the moon. In *Proceedings of the ION 2017 Pacific PNT Meeting*, pages 331–347, Honolulu, Hawaii, USA. Institute of Navigation (ION).

Fantinato, S., Miotti, E., Boschiero, M., Bartolucci, M., Bergamin, M., Marcantonio, D., Pulliero, M., Rozzi, F., Pozzobon, O., Facchinetti, C., et al. (2022). Development Challenges of a GNSS SDR Receiver for Moon Landing. In *Proceedings of the 35th International Technical Meeting of the Satellite Division of The Institute of Navigation (ION GNSS+ 2022)*, pages 602–627.

Iess, L., Di Benedetto, M., Boscagli, G., Racioppa, P., Sesta, A., De Marchi, F., Cappuccio, P., Durante, D., Molli, S., Plumaris, M. K., Tartaglia, P., Fienga, A., Rambeaux, N., Santi, F., Pastina, D., Linty, N., Sosnica, K., Bury, G., Zajdel, R., Belfi, J., Giordano, P., Swinden, R., and Ventura-Traveset, J. (2025). A Novel Orbit Determination and Time Synchronization Architecture for a Radio Navigation Satellite Constellation in the Cislunar Environment. *NAVIGATION: Journal of the Institute of Navigation*, 72(3).

Israel, D. J., Mauldin, K. D., Roberts, C. J., Mitchell, J. W., Pulkkinen, A. A., Cooper, L. V. D., Johnson, M. A., Christe, S. D., and Gramling, C. J. (2020). Lunanet: a flexible and extensible lunar exploration communications and navigation infrastructure. In *2020 IEEE Aerospace Conference*, pages 1–14.

Konitzer, L., Parker, J. J., Ashman, B., Esantsi, N., Facchinetti, C., Dovis, F., Minetto, A., Nardin, A., Bauer, F., Ansalone, L., et al. (2024). Science Objectives and Investigations for the Lunar GNSS Receiver Experiment (LuGRE). In *Proceedings of the 37th International Technical Meeting of the Satellite Division of The Institute of Navigation (ION GNSS+ 2024)*, pages 1061–1081.

Lemoine, F. G., Smith, D. E., Kunz, L., Smith, R., Pavlis, E. C., Pavlis, N. K., Klosko, S. M., Chinn, D. S., Torrence, M. H., Williamson, R. G., Cox, C. M., Rachlin, K. E., Wang, Y. M., Kenyon, S. C., Salman, R., Trimmer, R., Rapp, R. H., and Nerem, R. S. (1997). The development of the nasa gsfc and nima joint geopotential model. In Segawa, J., Fujimoto, H., and Okubo, S., editors, *Gravity, Geoid and Marine Geodesy*, pages 461–469, Berlin, Heidelberg. Springer Berlin Heidelberg.

Long, A. C. (2024). Goddard enhanced onboard navigation system (geons) mathematical specifications. Technical Publication NASA/TP-20240004259, NASA Goddard Space Flight Center, Greenbelt, Maryland. Release 3.0.

Mao, X., Arnold, D., Girardin, V., Villiger, A., and Jäggi, A. (2021). Dynamic GPS-based LEO orbit determination with 1 cm precision using the Bernese GNSS Software. *Advances in Space Research*, 67(2):788–805.

Minetto, A., Zocca, S., Vouch, O., Nardin, A., Dovis, F., Musmeci, M., and Facchinetti, C. (2025). LuNART-q: A quick-look navigation analysis and reporting tool for the LuGRE mission. In *ION GNSS+ 2025*, Baltimore, MD, USA.

Montenbruck, O. (2017). *Space Applications*, pages 933–964. Springer International Publishing, Cham.

Montenbruck, O. and Gill, E. (2000). *Satellite Orbits: Models, Methods, and Applications*. Springer, Berlin.

Montenbruck, O., Helleputte, T. V., Kroes, R., and Gill, E. (2005). Reduced dynamic orbit determination using GPS code and carrier measurements. *Aerospace Science and Technology*, 9(3):261–271.

Montenbruck, O., Kunzi, F., and Hauschild, A. (2021). Performance assessment of GNSS-based real-time navigation for the Sentinel-6 spacecraft. *GPS Solutions*, 26(1):12.

NASA (2024). Lunar reference frames. `https://www.nasa.gov/wp-content/uploads/2024/12/acr24-lunar-reference-frames.pdf`. Accessed: 2025-02-26.

Park, R. S., Folkner, W. M., Williams, J. G., and Boggs, D. H. (2021). The jpl planetary and lunar ephemerides de440 and de441. *The Astronomical Journal*, 161(3):105.

Parker, J., Dovis, F., Pozzobon, O., Facchinetti, C., Anderson, B., Ansalone, L., Ashman, B., Bauer, F. H., Bernardi, F., Boschiero, M., Campagnolo, G., D'Amore, G., Fantinato, S., Fiorina, F., Ghedin, M., Guzzi, S., Heighes, C., Impresario, G., Konitzer, L., Martini, D., McKim, S., Miller, J. J., Minetto, A., Miotti, E., Montini, N., Morichi, L., Musmeci, M., Nardin, A., Pino, T., Pulliero, M., Sanathanamurthy, S., Sciacca, L., Tedesco, S., Valencia, L., Varacalli, G., Vicari, D., Vouch, O., and Zocca, S. (2025a). Lunar GNSS Receiver Experiment (LuGRE) Mission Data.

Parker, J. J., Dovis, F., Anderson, B., Ansalone, L., Ashman, B., Bauer, F. H., D'Amore, G., Facchinetti, C., Fantinato, S., Impresario, G., et al. (2022). The Lunar GNSS Receiver Experiment (LuGRE). In *Proceedings of the 2022 International Technical Meeting of The Institute of Navigation (ION ITM 2022)*, pages 420–437.

Parker, J. J. K., Dovis, F., Konitzer, L., Esantsi, N., Ashman, B., Minetto, A., Nardin, A., Vouch, O., Zocca, S., Bernardi, F., Boschiero, M., Fantinato, S., Miotti, E., Facchinetti, C., Musmeci, M., and Varacalli, G. (2025b). GNSS Reception at the Moon: First Results of the Lunar GNSS Receiver Experiment (LuGRE). Manuscript submitted to *NAVIGATION*, Journal of the Institute of Navigation.

Schmidt, S. F. (1967). Compensation for modeling errors in orbit determination problems. Technical report, Analytical Mechanics Associates, Inc.

Selvan, K., Siemuri, A., Prol, F. S., Välisuo, P., Bhuiyan, M. Z. H., and Kuusniemi, H. (2023). Precise orbit determination of LEO satellites: a systematic review. *GPS Solutions*, 27(4):178.

Tedesco, S., Bernardi, F., Guzzi, S., Boschiero, M., Pulliero, M., Marcantonio, D., Ghedin, M., Miotti, E., Fantinato, S., Pozzobon, O., Facchinetti, C., Musmeci, M., D'Amore, G., Varacalli, G., Minetto, A., Dovis, F., Parker, J. J. K., McKim, S. A., Konitzer, L., Ashman, B., Sanathanamurthy, S., Miller, J. J., Valencia, L., and Bauer, F. (2023). Deep Space GNSS in Moon Transfer Orbit: the LuGRE Receiver. In *2023 IEEE International Conference on Wireless for Space and Extreme Environments (WiSEE)*, pages 1–6.

Vouch, O., Morichi, L., Zocca, S., Minetto, A., and Dovis, F. (2025). GNSS Precise Point Positioning in Cislunar Space: A Study on Regularized Least Squares and Availability. In *2025 IEEE/ION Position, Location and Navigation Symposium (PLANS)*, pages 1014–1025.

Vouch, O., Nardin, A., Minetto, A., Zocca, S., Dovis, F., Konitzer, L., Parker, J. J., Ashman, B., Bernardi, F., Tedesco, S., et al. (2024). Advancing Autonomous Navigation: Near-Moon GNSS-Based Orbit Determination. In *Proceedings of the 37th International Technical Meeting of the Satellite Division of The Institute of Navigation (ION GNSS+ 2024)*, pages 3277–3291.

Winternitz, L. B., Bamford, W. A., Long, A. C., and Hassouneh, M. (2019). GPS based autonomous navigation study for the lunar gateway. In *Annual American Astronautical Society (AAS) Guidance, Navigation, and Control Conference*, number AAS 19-096 in GSFC-E-DAA-TN66566.